

Changes of Extreme Wave Heights in Northern Hemisphere Oceans and Related Atmospheric Circulation Regimes

XIAOLAN L. WANG* AND VAL R. SWAIL

Climate Research Branch, Meteorological Service of Canada, Downsview, Ontario, Canada

(Manuscript received 27 September 1999, in final form 18 September 2000)

ABSTRACT

This study assesses trends in seasonal extremes (90- and 99-percentiles) of Significant Wave Height (SWH) in the North Atlantic and the North Pacific, as simulated in a 40-yr global wave hindcast using the National Centers for Environmental Prediction–National Center for Atmospheric Research reanalysis wind fields. For the last four decades, statistically significant changes in the seasonal extremes of SWH in the North Atlantic (NA) are detected only for the winter (January–March) season. These changes are found to be intimately connected with the North Atlantic oscillation (NAO). To be specific, significant increases of SWH in the northeast NA, matched by significant decreases in the subtropical NA, are found to be associated with an intensified Azores high and a deepened Icelandic low. This is consistent with the findings of previous studies based on different datasets. Changes in seasonal extremes of SWH in the North Pacific (NP) are found to be statistically significant for the winter and spring (April–June) seasons. Significant increases in the extremes of SWH in the central NP are found to be connected with a deeper and eastward extended Aleutian low. For both oceans, no significant trends of SWH are detected for the last century, though significant changes are found in the last four decades. However, multidecadal fluctuations are very noticeable, especially in the North Pacific.

1. Introduction

Analysis of wave and storm variability, and detection of climate changes therein, are of great importance to the operation and safety of shipping, offshore industries, and coastal development. In the related literature, there are many studies about the variability of storms/cyclones in the North Atlantic region (e.g., Schmith et al. 1998; Lambert 1996; Schinke 1993) and fewer studies about ocean waves.

However, in the past 3 yr three notable investigations of the trend and variability of ocean waves have been carried out. The first of these studies was that of Kushnir et al. (1997). That study involved a wave hindcast of only the North Atlantic Ocean (0–70°N), and covered only a relatively short 10-yr period (1980–89). The wave model was essentially the same as was used in the present study, and was driven by the European Centre for Medium-Range Weather Forecasts (ECMWF)

twice-daily operational 1000-hPa wind fields, on a 2.5° lat–long grid, adjusted to 20 m. The hindcast produced a monthly averaged significant wave height (SWH) history. A statistical extension of the results was carried out by relating the monthly mean SWH to monthly sea level pressure values derived from the ECMWF operational 1000-hPa analyses, using a Canonical Correlation Analysis (CCA) technique. As a result, a statistical hindcast of the monthly SWH was generated from historical sea level pressures derived from the Comprehensive Ocean–Atmosphere Data Set (COADS); this statistical hindcast was used to quantitatively estimate the systematic increase in wave heights over the period 1962–86. They found that an increasing trend in SWH at several northeast Atlantic locations since 1960 or so is related to the systematic deepening of the Icelandic low and intensification of the Azores high over the last three decades. Their analysis also suggests that wave height south of 40°N has decreased during the same period.

The hindcast carried out within the context of the European Union Waves and Storms in the Atlantic (WASA) program (WASA 1998; Gunther et al. 1998) used a third-generation (3G) wave model and spanned the continuous 40-yr period 1955–94. That hindcast also considered only the northeast Atlantic Ocean (38°–77°N, 30°W–45°E), and was driven by operational wind fields produced in real time by the U.S. Navy Fleet Numerical Meteorology and Oceanography Center

* Current affiliation: Network Strategies Division, Atmospheric Monitoring and Water Survey Directorate, Meteorological Service of Canada, Downsview, Ontario, Canada.

Corresponding author address: Network Strategies Division, Atmospheric Monitoring and Water Survey Directorate, Meteorological Service of Canada, 4905 Dufferin Street, Downsview, ON M3H 5T4 Canada.

E-mail: xiaolan.wang@ec.gc.ca

(FNMOC). The FNMOC wind fields were supplemented by Norwegian Meteorological Institute (DNMI) operational wind analyses in the extreme northeast Atlantic Ocean. Gunther et al. (1998) analyzed the hindcast for trends in annual mean and extreme wave patterns. However, inhomogeneities and other problems with the hindcast in the area west of 20°W limited the reliability of the analysis to the extreme eastern North Atlantic, where it was concluded that the wave climate has undergone significant variations on a timescale of decades. Part of that variability was found to be related to the North Atlantic oscillation (NAO). Increases in the annual 99-percentile significant wave height over the last 40 yr of about 3 cm yr⁻¹ (total change 1.2 m over 40 yr) were found for parts of the northeast Atlantic, north of the North Sea. Gunther et al. (1998) concluded that the DNMI analyses had suffered from an artificial worsening of the storm climate in data-sparse areas, and that minor inhomogeneities could be expected in the area between 70° and 40°N, and east of 20°W. Nevertheless, the WASA hindcast produced a well-validated reconstruction of the wave climate of the northeast Atlantic based on the best information and technology available at that time.

An unfortunate property of the earlier hindcast studies and of real-time NWP operations is that changes over time in data sources, improvements in data analysis techniques, and evolution and upgrades in numerical models have tended to impart a temporal or “creeping” inhomogeneity into the real-time products of such centers. When the wind fields produced by these centers are used to drive a wave model, these creeping inhomogeneities are translated into the wave climate simulations. Therefore, output data quality varies over time and subtle changes in climate may be masked. Such deficiencies in real-time analyses have led major centers to major attempts to produce a consistent analysis of the atmosphere through so-called “reanalysis” using historical atmospheric observations and current analysis schemes and NWP models.

A preliminary global atmospheric reanalysis produced at the ECMWF for the 15-yr period from 1979 to 1993 (ERA-15; Gibson et al. 1996) was used by Sterl et al. (1998) to make a global wave hindcast using the 3G WAM model, driven by the 10-m surface wind fields. They analyzed the linear trend of the monthly mean SWH for each calendar month over the 15-yr period. Large trends were found in January in the North Atlantic mean SWH (more than 1.2 m decade⁻¹), and in July in the ocean south of Africa (about 0.7 m decade⁻¹); the trends were found to vary greatly from month to month. For the winter (December–February; DJF) season in the North Atlantic, the trends were only about 0.4 m decade⁻¹ and were not statistically significant; this magnitude is similar to that from the entire WASA hindcast, although the center is displaced to the west (south of Iceland) in comparison with the WASA analysis. However, the WASA trend based on a com-

patible portion of the complete record, from 1975 to 1994, showed a decrease of about 2.0 cm yr⁻¹ in this area. Therefore, while the Sterl et al. (1998) hindcast represented a major advance in wind field quality and homogeneity, it is for a period too short to confirm a significant change in the global wave climate.

As we have shown, previous wave hindcasts suffer from a number of critical deficiencies, in that they either 1) cover a relatively short period of time; 2) are limited to the North or Northeast Atlantic; or 3) use wind input that is of relatively poor quality (as compared with reanalyses), or contains inhomogeneities, or both. The wave hindcast analyzed in the present study is global and covers a relatively long period of 40 yr (1958–97). The wave hindcast is derived from the National Centers for Environmental Prediction (NCEP)–National Center for Atmospheric Research (NCAR) reanalysis project (hereinafter NRA; Kalnay et al. 1996) wind fields, using a second-generation wave model. More specific, a deep-water version of the so-called ODGP2 (see section 2) fully discrete spectral ocean wave model (Khandekar et al. 1994) was used to incorporate the 40-yr (1958–1997) history of global 6-h 10-m wind fields, derived from the NRA surface wind fields, to generate comprehensive numerical hindcasts of SWH in oceans over the globe for the same 40-yr period. The NRA wind fields and the resulting wave hindcast should possess better homogeneity over time than previous hindcasts and, hence, are more suitable for trend analysis.

The purpose of the present study is twofold. First, we will verify whether our wave hindcast leads to conclusions similar to those of previous studies using a different wave model forced by a different atmospheric dataset. Second, we will also analyze seasonal extremes of significant wave height in the North Pacific Ocean in more detail, while so far more attention has been drawn to the North Atlantic. We conducted the analysis for the North Atlantic and the North Pacific, separately.

Unlike the previous studies, which mostly analyzed the intramonthly percentiles or monthly means of SWH, we analyzed seasonal extremes in terms of seasonal 90- and 99-percentiles of SWH. The statistical methods used in this study are also slightly different from the ones used in the previous studies. We first use the Mann–Kendall test to assess linear trends of SWH extremes on seasonal timescales, since the least squares estimator of trend (i.e., b in the linear regression $Y_t = a + bt + \varepsilon_t$, where ε_t is a white noise process) is vulnerable to gross errors and the associated confidence interval is sensitive to nonnormality of the parent distribution (Sen 1968). We also take into account the effect of autocorrelation when assessing trends and their significance level. We then adopt a statistical approach, called Redundancy Analysis (RA), to characterize the links between the large-scale variability of SWH extremes and large-scale atmospheric circulation (SLP) patterns [as represented by the leading Principal Components (PCs) of the relevant fields], which are further used to extend the

numerical hindcasts back to January 1899, providing a best guess of the historical variability of SWH extremes. Here, the use of the least squares technique RA is reasonable despite the local non-Gaussian behavior of the SWH extremes. This is due to the fact that the large-scale variability of the SWH field, as captured in the first 7 PCs (cf. section 3), is not significantly non-Gaussian, as suggested by the Kolmogorov–Smirnov test (most of the leading PCs are not significantly non-Gaussian at the 5% level, with a few being not significantly non-Gaussian at a slightly lower level).

For comparison, we also carried out similar analyses on seasonal extremes of wind speed. However, only a brief discussion of the wind results will be included in this study.

In section 2 we give a brief description of the wave hindcast model and methodology. Section 3 briefly describes the datasets and statistical analysis procedures used in this study. We then present and discuss the results of our analyses in section 4. We complete this study in section 5 with a summarizing discussion, comparing our results with those of the related previous studies.

2. The global wave hindcast

The wind fields used in the generation of the global wave hindcast were the NRA 6-h 10-m wind fields. The only adjustment made to the original NRA wind fields for this hindcast was an adjustment to neutral stability, using the technique described by Cardone et al. (1996). The stability information required by that technique was derived from the NRA 2-m temperature and sea surface temperature fields. These neutrally stable NRA wind fields were previously evaluated by Swail and Cox (2000) and found to produce very good wave hindcasts for the North Atlantic when compared with buoy wave measurements.

The wave model used in this global hindcast consists of the deep-water ODGP2 spectral growth–dissipation algorithm coupled with a global wave propagation system with great-circle propagation effects included (Greenwood et al. 1985). The ODGP2 wave model is a second-generation (2G) formulation of the original Ocean Data Gathering Program (ODGP) model developed by Cardone et al. (1976). The spectrum is resolved into 24 directional bins and 23 frequency bins.

In the hindcast procedure, wind fields are updated at 6-h intervals and the model time step is 3 h. Output wind and wave fields are archived at 6-h intervals at all model grid points. The ice field was specified on a monthly basis, using long-term mean monthly historical ice concentration data. Grid points at which the ice concentration is 5/10 or greater are treated as land.

For this hindcast, the ODGP2 wave model was adapted on a global grid spacing of $1.25^\circ \text{ lat} \times 2.5^\circ \text{ long}$. Most marginal seas are resolved, though smaller bays and straits such as Gibraltar and Malacca are not.

The ODGP2 wave model is described in detail most

recently in Khandekar et al. (1994); detailed evaluation of the model, using NRA wind fields, is given by Cox and Swail (2001). That study evaluated the skill of the wave hindcast using in situ and satellite wind and wave datasets and also assessed the long-term climatology of the wave hindcast. Their evaluation showed excellent agreement in terms of bias and scatter between the measurements and the hindcast over the entire 40-yr period. Altimeter wind and wave measurements provide the best global spatial coverage to evaluate the ODGP2 wave hindcast and are an independent assessment since they were not assimilated in the NRA. Statistics and plots from the individual instruments (*ERS-1*, *ERS-2*, and *TOPEX*) showed very good agreement among each other, so the datasets were combined for these comparisons. Figure 1 shows quantile–quantile (Q–Q) scatterplots of the combined altimeter for the complete period of the satellite record versus the ODGP2 wave hindcast (more than 2 million comparisons). There is excellent agreement over the entire range of the frequency distribution for model versus measured waves; the winds compare well up to about 15 m s^{-1} , after which the measured winds are increasingly low. This is most likely due to a wind speed saturation problem in altimeter wind speeds, since it is not apparent in the in situ winds. Northern Hemisphere statistics show biases (hindcast–measured) for waves of 0.02 m, with a scatter index of 0.26. Similar statistics were found for high-quality Canadian and U.S. buoy wave data, with bias of 0.10 m and scatter index of 0.27. The skill of this model has also been documented in numerous studies, most recently by Cardone et al. (1996) and Cardone and Resio (1998). These studies indicate that the recent 3G formulations provide no discernible increase in skill in specification of SWH over that of ODGP2 in sea states up to SWH of 12 m. Above SWH of about 12 m, all models tended to underspecify peak storm SWH. However, it should be noted that for the purpose of the global hindcast any deficiency of hindcasts for such rare extreme storm seas should not affect the quality of the hindcast or the derivative wave height climate statistics analyzed in this paper with regard to global wave climate, its variability and trend, since the upper limit of the SWH distribution analyzed in this paper, that is, the 99-percentile, is about 9 m even in the harshest wave climate and this is well within the range of demonstrated accuracy of the ODGP2 model in general and of the global hindcast specifically.

3. Datasets and procedures

The primary purpose of this study is to assess linear trends in the seasonal 90- and 99-percentiles of SWH. We conducted the analysis for the North Atlantic (80°W – 20°E , 20° – 70°N) and the North Pacific (120° – 270°E , 20° – 70°N), separately. The seasonal extremes (90- and 99-percentiles) of SWH are derived from the 40-yr (1958–97) numerical wave hindcast described in

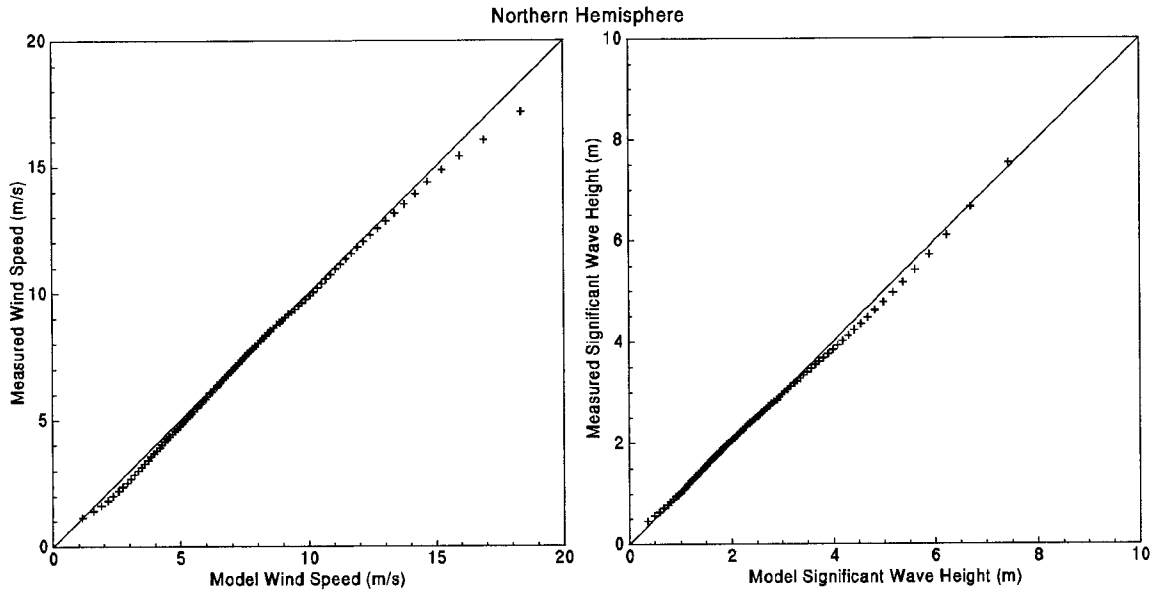


FIG. 1. Quantile–quantile (from 1% to 99%) wind speed (m s^{-1}) and wave height (m) comparisons of the ODGP2 wave hindcast and altimeter measurements for Northern Hemisphere (20° – 70°N , after Cox and Swail 2001).

TABLE 1. The fractions of variance explained by the retained EOFs of the mean sea level pressure (SLP) fields (P_{SLP}) or the SWH extremes (P_{SWH}) for each season, as well as the overall redundancy index R and the redundancy indices associated with the first five best predicted modes (R_j , $j = 1, 2, \dots, 5$). The numbers in square brackets are the correlations between the relevant predictor and predictand time series.

		P_{SLP}		P_{SWH}	R	R_1	R_2	R_3	R_4	R_5	
NA	Winter	92.2	H_{90}	82.4	0.547	0.328	0.125	0.042	0.022	0.017	
			H_{99}	69.6	0.464	[0.818]	[0.815]	[0.506]	[0.305]	[0.442]	
	Spring	83.4	H_{90}	67.9	0.289	0.271	0.083	0.049	0.031	0.015	
			H_{99}	62.4	0.270	[0.790]	[0.694]	[0.589]	[0.013]	[0.196]	
	Summer	87.3	H_{90}	73.1	0.524	0.158	0.059	0.023	0.017	0.015	
			H_{99}	61.7	0.382	[0.593]	[0.438]	[0.328]	[0.082]	[0.024]	
	Autumn	93.1	H_{90}	73.4	0.499	0.095	0.065	0.040	0.029	0.022	
			H_{99}	62.4	0.405	[0.435]	[0.389]	[0.555]	[0.341]	[0.095]	
	NP	Winter	89.3	H_{90}	76.7	0.587	0.263	0.092	0.072	0.043	0.035
				H_{99}	63.0	0.482	[0.798]	[0.454]	[0.285]	[0.307]	[0.242]
		Spring	77.8	H_{90}	69.3	0.386	0.203	0.064	0.051	0.024	0.021
				H_{99}	60.4	0.305	[0.694]	[0.134]	[0.327]	[0.197]	[0.150]
Summer		83.1	H_{90}	68.8	0.435	0.211	0.160	0.062	0.024	0.020	
			H_{99}	59.8	0.439	[0.555]	[0.670]	[0.529]	[0.428]	[0.309]	
Autumn		91.3	H_{90}	64.9	0.485	0.167	0.120	0.060	0.025	0.017	
			H_{99}	59.0	0.382	[0.615]	[0.614]	[0.539]	[0.053]	[0.050]	
Winter		89.3	H_{90}	76.7	0.587	0.371	0.072	0.061	0.033	0.026	
			H_{99}	63.0	0.482	[0.866]	[0.661]	[0.677]	[0.450]	[0.385]	
Spring		77.8	H_{90}	69.3	0.386	0.303	0.078	0.036	0.024	0.021	
			H_{99}	60.4	0.305	[0.833]	[0.628]	[0.557]	[0.384]	[0.276]	
Summer	83.1	H_{90}	68.8	0.435	0.156	0.074	0.063	0.041	0.027		
		H_{99}	59.8	0.439	[0.545]	[0.425]	[0.540]	[0.006]	[0.284]		
Autumn	91.3	H_{90}	64.9	0.485	0.128	0.063	0.037	0.033	0.023		
		H_{99}	59.0	0.382	[0.537]	[0.065]	[0.313]	[0.303]	[0.018]		
Winter	89.3	H_{90}	76.7	0.587	0.147	0.094	0.077	0.055	0.039		
		H_{99}	63.0	0.482	[0.650]	[0.708]	[0.477]	[0.395]	[0.352]		
Spring	77.8	H_{90}	69.3	0.386	0.175	0.102	0.073	0.035	0.029		
		H_{99}	60.4	0.305	[0.616]	[0.596]	[0.635]	[0.510]	[0.241]		
Summer	83.1	H_{90}	68.8	0.435	0.206	0.096	0.069	0.053	0.038		
		H_{99}	59.8	0.439	[0.786]	[0.726]	[0.564]	[0.356]	[0.312]		
Autumn	91.3	H_{90}	64.9	0.485	0.144	0.085	0.077	0.038	0.020		
		H_{99}	59.0	0.382	[0.763]	[0.563]	[0.548]	[0.373]	[0.228]		

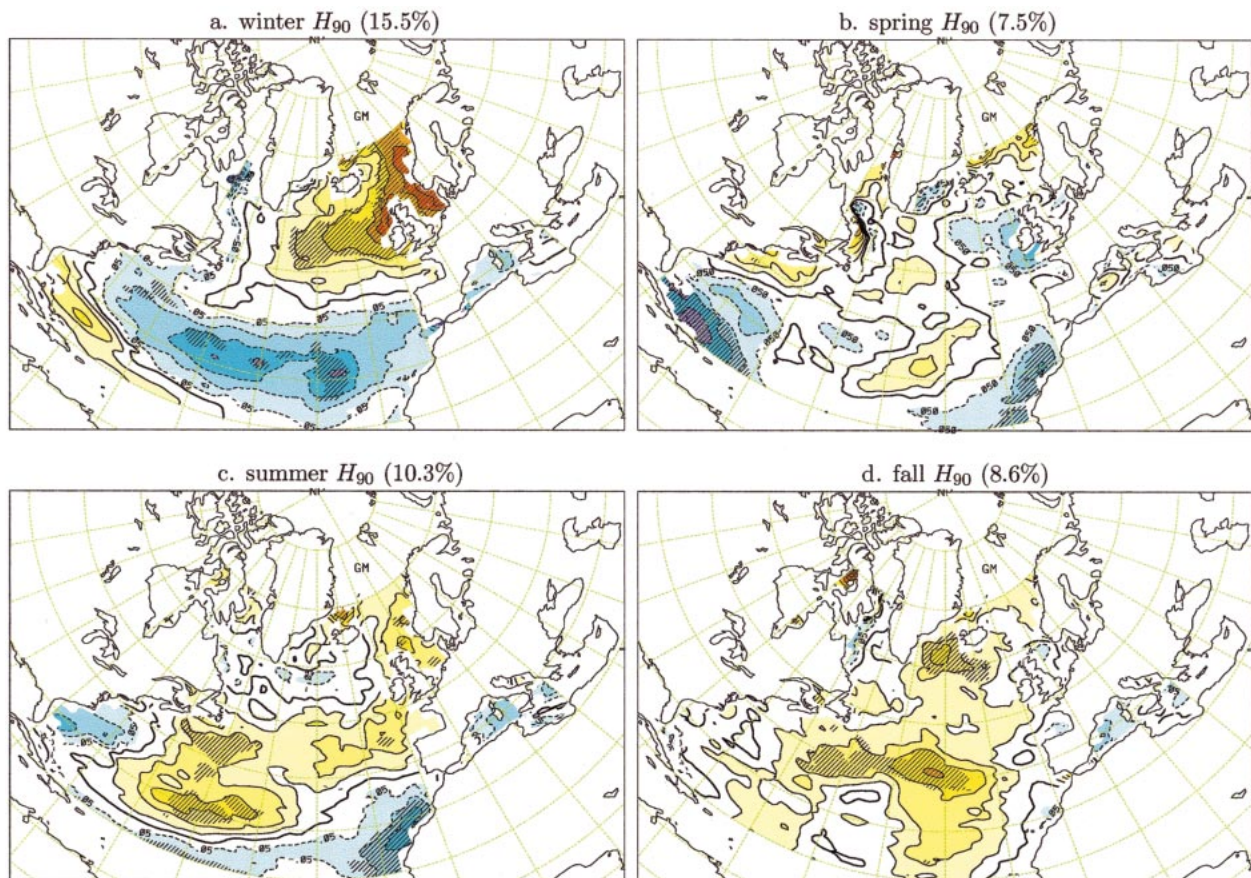


FIG. 2. Changes of the seasonal 90-percentiles of SWH (H_{90}), expressed as percentages of the 40-yr mean H_{90} . The contour interval is 0.05 (i.e., 5%) per 40 yr. Solid, bold, and dashed lines are positive, zero, and negative contours, respectively. Hatching indicates areas of significant changes. The numbers in parentheses are the rejection rates of the Mann–Kendall test.

section 2. For the sake of convenience, JFM is defined as winter, AMJ as spring, July–September (JAS) as summer, and October–December (OND) as autumn. For each region, the data used in this study mainly consist of

- 40 seasonal 90-percentiles of SWH (H_{90}) in the ocean for each season covering the 40-yr period from 1958 to 1997;
- 40 seasonal 99-percentiles of SWH (H_{99}) in the ocean for each season covering the same 40-yr period; and
- 99 seasonal means of SLP covering the region for each season in the 99-yr period from 1899 to 1997, taken from the NCAR dataset ds010.1 (Trenberth and Paolino 1980).

The SWH data are on a $1.25^\circ \text{ lat} \times 2.50^\circ \text{ long}$ grid, while the SLP data are on a $5^\circ \text{ lat} \times 5^\circ \text{ long}$ grid. The seasonal statistics are calculated from 6-h data of SWH for the specific season (364–368 data per season).

First of all, the Mann–Kendall test for trend against randomness (Mann 1945; Kendall 1955) was carried out for the time series of SWH extremes at each grid point in the grid, separately. The effect of autocorrelation was

also taken into account. The procedures of trend analysis in this study are detailed in appendix A. Since the Mann–Kendall test is carried out at each grid point, separately, the rejection rate (i.e., the percentage of areas where the null hypothesis that the time series in question is random is rejected) can serve as a measure of field significance of trend. The number of degrees of freedom of the large-dimension SWH fields cannot exceed 40 (i.e., the length of the time series analyzed here). Actually, the first 30 empirical orthogonal functions (EOFs)/PCs of the SWH extremes account for more than 95% of the total variance. Thus, the number of degrees of freedom seems unlikely to exceed 30. According to Livezey and Chen (1983), for a field of 40, 30, and 20 degrees of freedom, one would expect, by accident, a rejection rate of about 12.5%, 13.5%, and 17.0%, respectively, if the test is conducted at the 5% significance level (which is the case of the present study). Therefore, in this study trend could be field significant at the 5% level only if the rejection rate is greater than 12.5%.

The Mann–Kendall test was also performed on the Principal Components (PCs) of the SWH extremes fields to further assess the relative importance of the trend components detected.

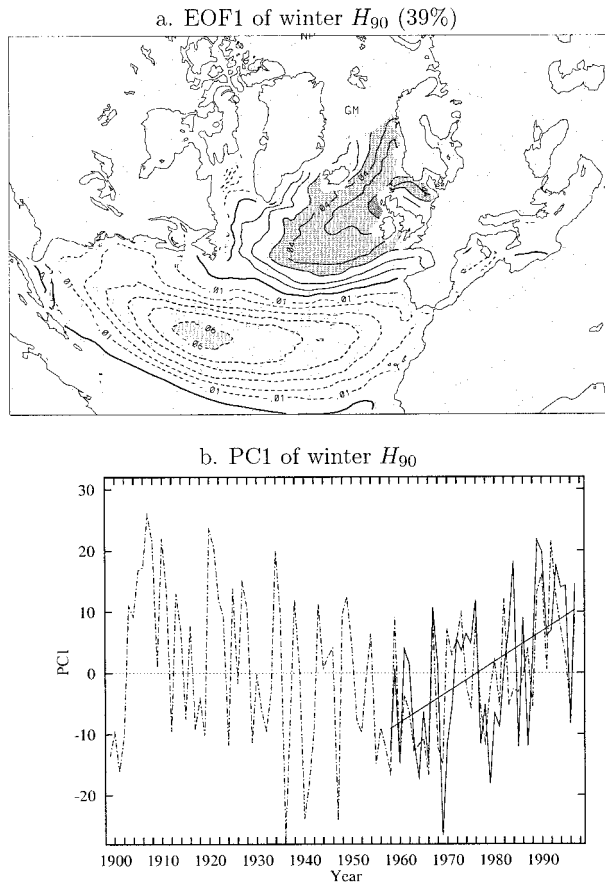


FIG. 3. The EOF1 and PC1 of winter seasonal 90-percentiles of SWH (H_{90} , m). (a) The contour interval is 0.01; solid, bold, and dashed lines are positive, zero, and negative contours, respectively. The number in parentheses is the portion of the variance explained by the EOF1/PC1 of the corresponding numerical hindcast. (b) The solid curve represents the PC1 of the numerical hindcast, and the dashed curve, the PC1 of the statistical reconstruction. The trend shown was estimated from the PC1 of the numerical hindcast.

Last, changes of the ocean wave extremes are related to changes in the atmospheric circulation at sea level by means of Redundancy Analysis—a technique that can be used to associate patterns of variation in a predictor field with patterns of the predictand fields (see appendix B). Since the dimensionality of the SWH and SLP grids is large, it is imperative to compress the data for RA by projecting them onto a few representative EOFs. For each region, we estimated the EOFs of the SWH extremes and SLP data for each season, separately. Taking into account the length of the time series in question and looking at the relevant spectrum of eigenvalues (trying to truncate modes at the last clear break in the slope of each eigenvalue curve), we decided to retain seven leading EOFs/PCs to represent the relevant original field time series. For each variable, Table 1 gives the percentages of the total variance associated with the corresponding retained EOFs/PCs for each season. Having determined the EOF truncation, we use the

retained PCs of a seasonal SWH statistic (H_{90} or H_{99}) as the predictand, and the retained PCs of seasonal mean SLP over the region as the predictor. For the regression model in RA (cf. appendix B), the training datasets consist of the SLP and SWH data for the 40-yr period from 1958 to 1997. The statistical forecasts are cross-validated by withholding data for years $(y - 1)$, y , $(y + 1)$ when predicting year y . The statistical reconstructions for years 1899–1957 are derived from the same regression model as for year 1958.

4. Trends in seasonal extremes of SWH and the related circulation regimes

In this study, changes of seasonal SWH extremes (H_{90} and H_{99}) in the 40-yr period (1958–97) are expressed as percentages of the 40-yr mean of the corresponding SWH extremes. The rate of actual changes (in meters) will be given for some areas of particular interest but the related maps are not shown in this paper. Unless otherwise specified, significant trends indicate trends identified at the 95% confidence level. In the following two subsections, we describe the changes of SWH in the North Atlantic (NA) and in the North Pacific (NP), sequentially.

a. The North Atlantic

Figure 2 shows the results of performing trend analysis on the 1958–97 time series of seasonal 90-percentiles of SWH (H_{90}) at each grid point in the North Atlantic, separately. For the four seasons of the year, changes of H_{90} are found to be most significant in the winter season. As shown in Fig. 2a, highly significant increases of H_{90} are identified for the northeast North Atlantic in winter, the rate of increase being 10%–35% (40–204 cm) per 40-yr. Such increases are accompanied by significant decreases in the subtropical North Atlantic. Changes of H_{90} are much less significant in the other seasons, being least significant in the spring season. The trend pattern of spring H_{90} features two small areas of significant decreases, one in the southwest corner of the North Atlantic, another in the ocean off the African coast (cf. Fig. 2b). In the summer season, as shown in Fig. 2c, significant increases in the central subtropical North Atlantic are matched by significant decreases in the ocean off the African coast. In the autumn season, the trend pattern of H_{90} is characterized by significant increases in central and northern North Atlantic, as shown in Fig. 2d. However, the rejection rates of the Mann–Kendall tests, listed in Table 2, indicate that only the changes identified for the winter season are of field significance (cf. the second paragraph of section 3).

For each season, we also apply the trend analysis technique to each PC of the wave extremes, separately. Significant trends are identified only in the PC1 of the winter H_{90} , and in the PC3 and PC7 of the summer H_{90} . Significant trends are not found in the leading PCs of

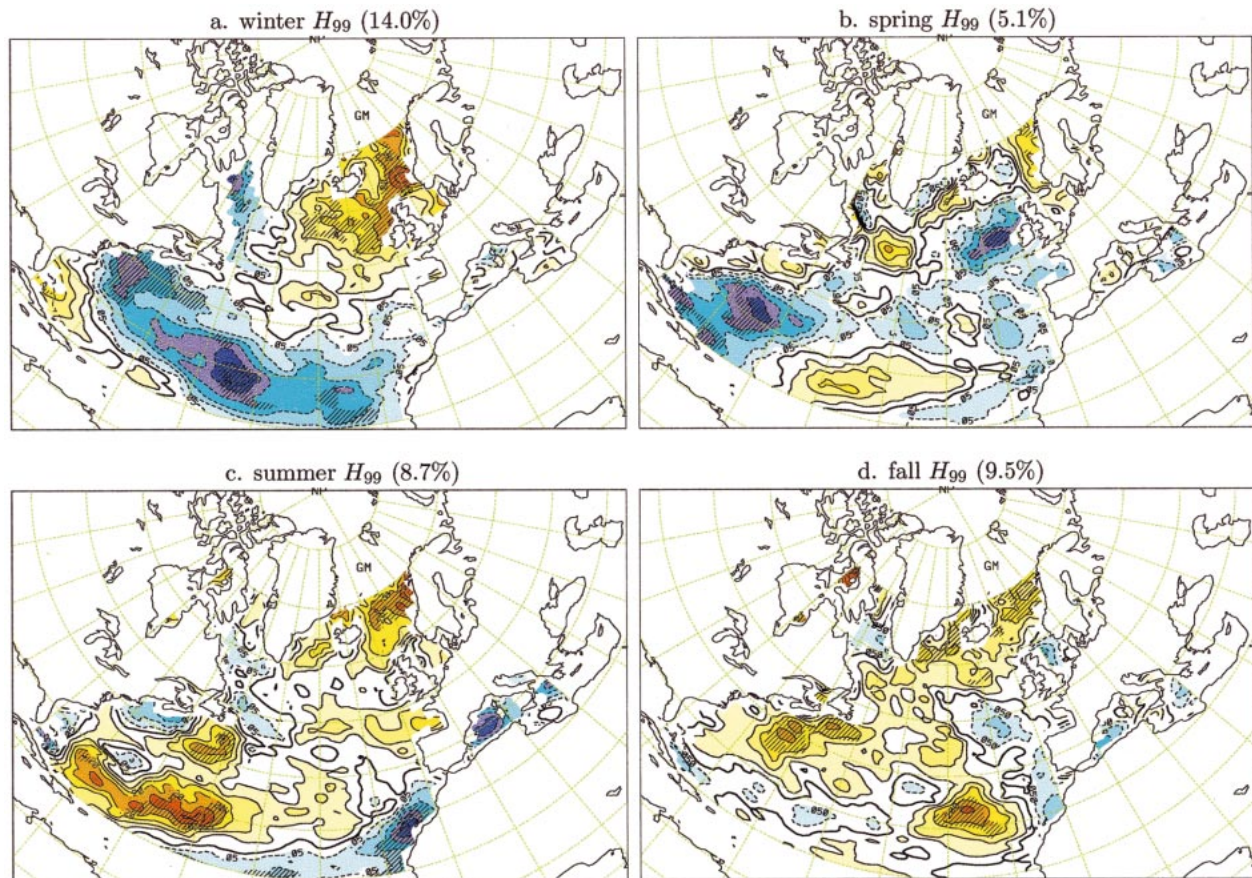


FIG. 4. The same as in Fig. 2 but for changes in the seasonal 99-percentiles of SWH (H_{99}), expressed as percentages of the 40-yr mean H_{99} .

H_{90} for the spring and autumn seasons. Moreover, no significant SLP changes are found (in the subsequent RA) to be connected with the changes of summer H_{90} . Thus, the trends identified for the summer H_{90} are considered to be trivial and/or unreliable and are hence ignored hereinafter. The seasonal 90-percentiles of SWH are found to have significant trends only in the winter season. The trend components are well represented by the EOF1/PC1 of the winter H_{90} : as shown in Fig. 3, the EOF1 is similar to the trend pattern shown in Fig. 2a, while the increasing trend in the associated PC1 corresponds to increases in the northeast North Atlantic and decreases in the subtropical North Atlantic.

For the seasonal 99-percentiles of SWH (H_{99}), similarly, changes are found to be most significant in winter and least significant in spring (cf. Fig. 4). The rejection rates (cf. Table 2) indicate that only the trends identified for the winter season might be field significant. In other seasons, trends can be considered as trivial and/or unreliable. As shown in Fig. 4a, the trend pattern of winter H_{99} features significant increases in the northeast North Atlantic that are matched by significant decreases in the subtropical North Atlantic. Again, as can be inferred from Fig. 5, such trend components of winter H_{99} are

well represented by the relevant EOF1/PC1. The PC1 possesses a significant increasing trend. No significant trends are found in other PCs of winter H_{99} .

Generally, changes identified for H_{99} appear to be less significant than those identified for the H_{90} counterpart, especially in the northeast North Atlantic. However, comparison of Fig. 4a with Fig. 2a reveals that the 99-percentiles of SWH in the ocean off the North America coast possess a much more notable decreasing trend (larger amplitude and higher significance level) than its 90-percentiles counterpart. This indicates that the ocean off the North America coast has become less variable, experiencing lower wave extremes in the winter season during the last four decades.

As described in section 2, the RA technique is used in this study to link changes of SWH extremes with changes in the sea level pressure (SLP). The SWH and SLP datasets are represented by seven leading EOFs/PCs of the relevant fields. Here, the leading PCs of SLP are used as predictors \mathbf{X} to forecast the seasonal extremes of SWH (predictand \mathbf{Y}). For each seasonal statistic of SWH (H_{90} and H_{99}) in the 1958–97 period, Table 1 gives the proportion of the total variance of SWH extremes that is connected with variations in the

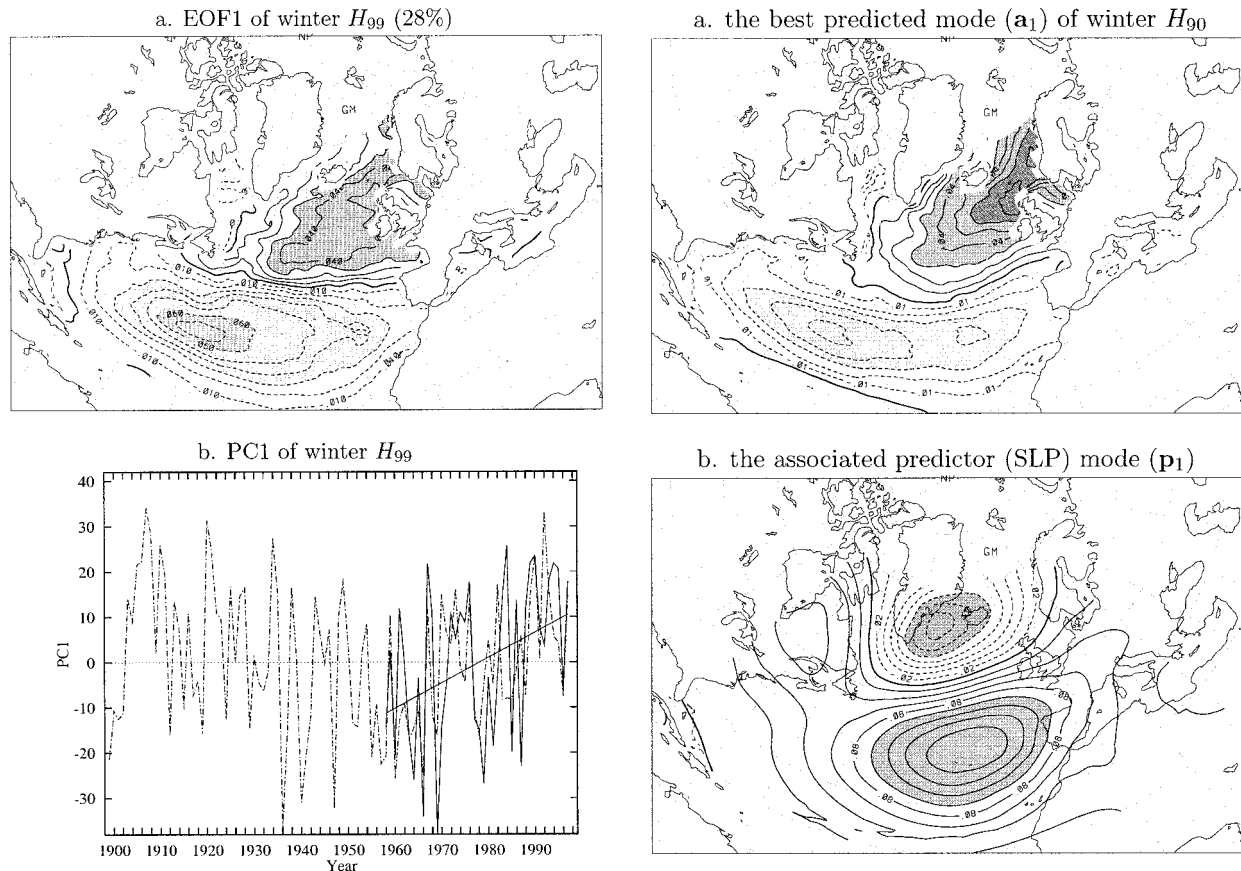
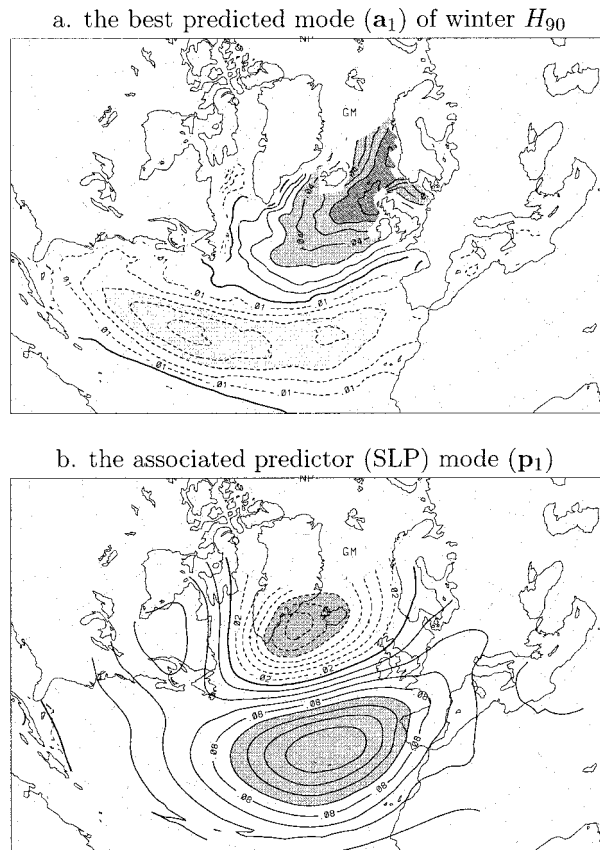


FIG. 5. The same as in Fig. 3 but for the EOF1 and PC1 of winter seasonal 99-percentiles of SWH (H_{99} , m).

SLP field (i.e., the overall redundancy index in column R). This proportion is always greater in winter than in the other seasons, and for the 90-percentiles (H_{90}) than for the 99-percentiles (H_{99}) counterpart. These indicate that it is easier to predict the SWH extremes in winter, and that the 90-percentiles are easier to predict than the 99-percentiles, given SLP as the predictor. The most important association between ocean waves and SLP is represented by the first pair of predictor and predictand modes, which often accounts for more than 50% of the total relationship in terms of the predictand variance (cf. columns R and R_1 in Table 1).

Figure 6 shows the first pair of predictand (winter H_{90}) and predictor (SLP) modes, as well as their temporal variations (normalized time series). The best predicted mode \mathbf{a}_1 , which accounts for about 27% of the total H_{90} variance in winter, resembles the trend pattern shown in Fig. 2a and the EOF1 shown in Fig. 3; while the predictor (SLP) mode has a structure like the so-called NAO, explaining some 26% of the total variance of winter seasonal mean SLP. For the 1958–97 period, both the predictor and predictand time series (i.e., SLP-T1 and H_{90} -T1 in Fig. 6) possess a significant increasing trend, which indicates that the observed deepened Icelandic low and intensified Azores high result in in-



c. Temporal variations of modes \mathbf{a}_1 and \mathbf{p}_1

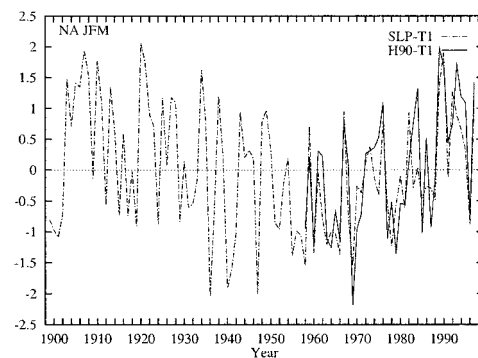


FIG. 6. The best predicted mode of winter seasonal 90-percentiles of SWH (H_{90}) in the North Atlantic and the associated predictor (SLP) mode. In the 1958–97 period, both the predictor and the predictand time series (SLP-T1 and H_{90} -T1; normalized) have a significant increasing trend.

creases of winter H_{90} in the northeast North Atlantic and decreases in the subtropical North Atlantic. Moreover, both time series are highly significantly correlated with the simultaneous winter seasonal NAO index, which is based on the difference of normalized SLP between Ponta Delgada, Azores, and Stykkisholmur/Reykjavik, Iceland (Hurrell 1995). The correlation is 0.875 for SLP-T1, and 0.909 for H_{90} -T1. These indicate

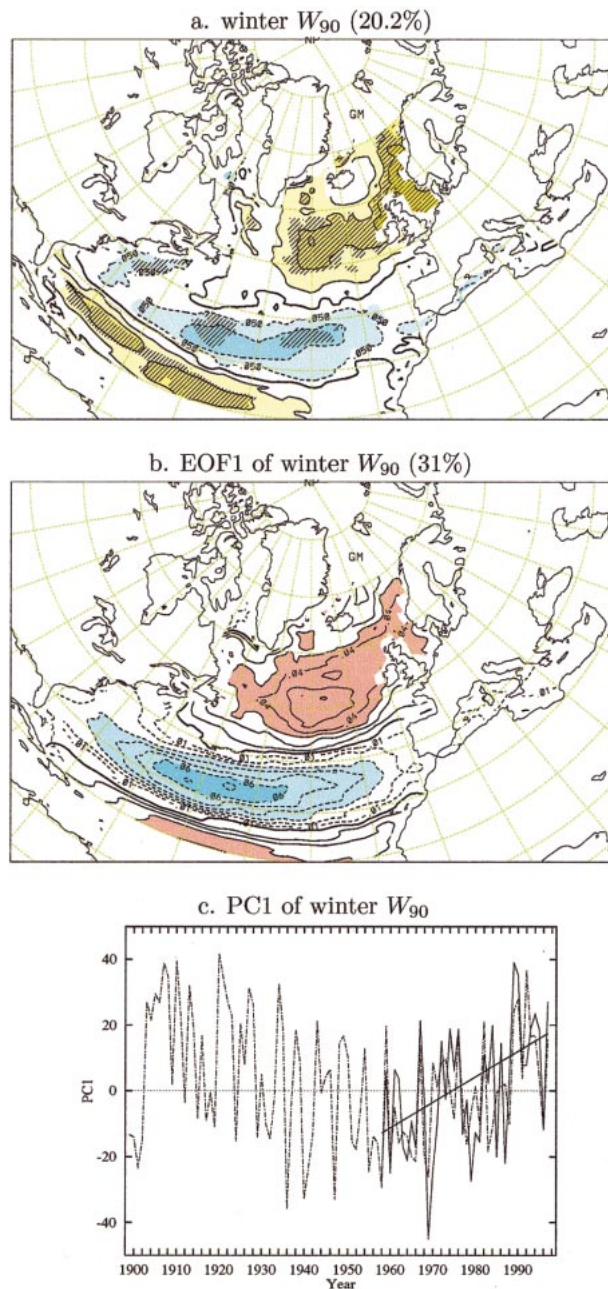


FIG. 7. (a) The same as in Fig. 2 but for changes of the winter seasonal 90-percentiles of wind speed (W_{90}), expressed as percentages of the 40-yr mean W_{90} . (b) and (c) The same as in Fig. 3 but for the EOF1 and PC1 of the winter W_{90} (m s^{-1}).

that the significant changes of winter H_{90} in the last four decades are closely connected with the significant changes in the NAO variations. No significant trends are found in the time series of other pairs of predictor and predictand modes.

For the winter H_{99} , similarly, the best predicted mode resembles the relevant trend pattern and EOF1, the predictor (SLP) mode possesses an NAO-like structure, and both the predictor and predictand time series have a

significant increasing trend (figures are quite similar to those shown in Fig. 6 and hence are not shown here). Again, the correlation between the predictand (predictor) time series and the simultaneous winter seasonal index of NAO is 0.865 (0.887), which is highly significant. These again indicate that the significant changes in winter H_{99} are associated with the NAO variations.

Since the SLP data cover the period from 1899 to 1997, the cross-validated RA linear predictions \hat{Y} (i.e., the reconstructed PCs of SWH extremes) can be extended back to 1899. By doing so, we statistically extend the numerical hindcast of the SWH extremes back to 1899. These statistically reconstructed PCs of SWH extremes provide a best guess of the temporal variations of the SWH extremes in the last century. These statistical hindcasts can be considered homogeneous because the SLP dataset used here is mainly homogeneous over the North Atlantic (Schmith et al. 1998). In the last four decades, the reconstructed time series are in good agreement with the corresponding numerical hindcasts. For example, as shown in Figs. 3b and 5b, the statistically reconstructed PC1s of winter H_{90} and H_{99} agree well with the corresponding “numerically hindcasted” PC1s (i.e., the PC1s derived from the SWH extremes of the 40-yr numerical hindcasts), the correlation between the reconstructed and hindcasted PC1s being 0.65 and 0.54, respectively. Note that the PC1/EOF1 well represent the trend components in the oceanic wave extremes. For the northeast North Atlantic, the reconstructed PC1s appear to possess a decreasing trend up to the 1950s while confirming the numerically hindcasted increases in the last four decades. However, significant trends are not found in the reconstructed PCs for the entire last century. The present SWH extremes appear to be comparable with those at the beginning of this century, similar to the results found by the WASA Group (1998). Thus, the significant trends identified in both the SLP data and the seasonal SWH extremes for the last four decades may well be due to the natural long-term fluctuation.

As to the corresponding wind speed extremes, we obtained similar results: significant trends are found only in the seasonal extremes (90- and 99-percentiles) of wind speed in the winter season. These trend components are also well represented by the relevant EOF1/PC1. As shown in Fig. 7, for example, the trend pattern of the 90-percentiles (W_{90}) resembles the relevant EOF1, while the associated PC1 has a significant increasing trend, representing significant increases of the winter W_{90} over the northeast North Atlantic that are matched by significant decreases over the midlatitudes of North Atlantic. In the related RA, similarly, such trends were found to be closely related to the NAO variability. However, there are differences between the trend pattern here and the one shown in Fig. 2a: significant increases were found for the 90-percentiles of wind speed over the subtropical North Atlantic (south of 30°N), but no significant changes are identified for the SWH counterpart. Also, in the northeast North At-

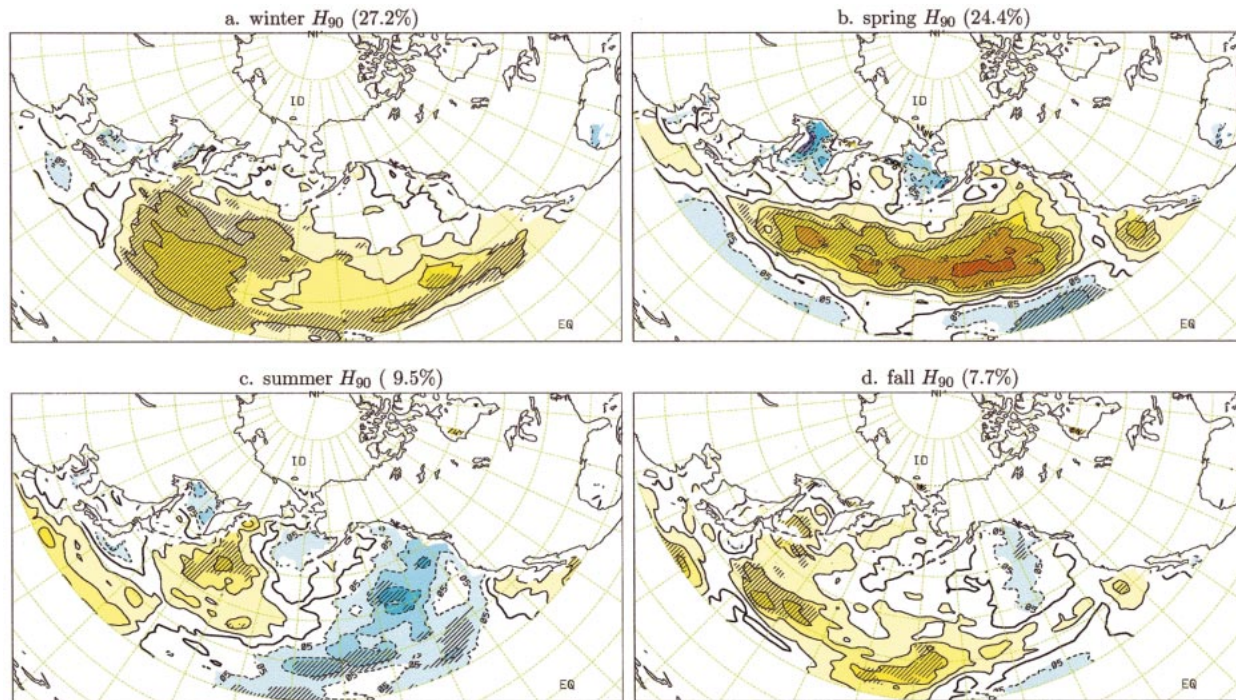


FIG. 8. The same as in Fig. 2 but for changes of the seasonal 90-percentiles of SWH (H_{90}) in the North Pacific, expressed as percentages of the 40-yr mean H_{90} .

lantic, the rates of increase in SWH extremes are much greater than those identified for the wind speed extremes, as would be expected.

b. The North Pacific

The results of performing trend analysis on the 1958–97 time series of seasonal 90-percentiles of SWH (H_{90}) at each grid point in the North Pacific are shown in Fig. 8. The rejection rates (listed in Table 2) suggest that the H_{90} trends could be field significant in both the winter and spring seasons. Another difference from the North Atlantic H_{90} is that the largest rates of increase (in percentage of the mean) are now found in the spring season rather than in the winter season, though significant increases of 10%–20% (40–126 cm) per 40-yr are also identified for winter (cf. Fig. 8a). In the spring season, as shown in Fig. 8b, increases of 10%–30% (40–104 cm) are found to be significant in the central North Pacific, which are matched by significant decreases of 10%–15% (up to 40 cm) in the subtropical North Pacific and in the western Okhotsk Sea. Changes are much less significant in the summer and autumn seasons. The trend pattern of summer H_{90} is characterized by significant increases in the northwest North Pacific that are accompanied by significant decreases in the eastern North Pacific (cf. Fig. 8c); while the trend pattern of fall H_{90} features significant increases in the western subtropical North Pacific (cf. Fig. 8d).

Significant trends are also found in PC3 and PC5 of

winter H_{90} , in PC1 of spring H_{90} , and in PC4 of autumn H_{90} . Also, the PC1 of winter H_{90} is found to have a trend that is significant at the 90% confidence level. Since no significant changes of SLP are found to be associated with the changes identified for the autumn H_{90} , while significant SLP changes are identified to be linked with the H_{90} changes in the spring and winter seasons, we will hereinafter focus on the trends identified for the spring and winter seasons.

The EOF1 of the spring H_{90} is shown in Fig. 9, together with the associated PC1. Apparently, the EOF1 resembles the trend pattern shown in Fig. 8b; and the significant increasing trend in the PC1 indicates remarkable increases in the central North Pacific.

For the H_{99} , the rejection rates (cf. Table 2) indicate that the changes might be of marginal field significance only in the winter and spring seasons. Figure 10a shows the trend pattern of H_{99} in spring: significant increases of 15%–35% (80–225 cm) per 40 yr are observed in the central North Pacific. The trend components are also well represented by the EOF1/PC1. As shown in Fig. 11, the EOF1 resembles the trend pattern shown in Fig. 10a, the associated PC1 possesses a significant (at the 90% confidence level) increasing trend, indicating significant increases in the spring H_{99} over the central North Pacific.

Figure 12 shows the best predicted mode of the spring H_{90} and the associated predictor (SLP) mode, as well as their temporal variations. The best predicted mode, which accounts for about 11% of the total H_{90} variance

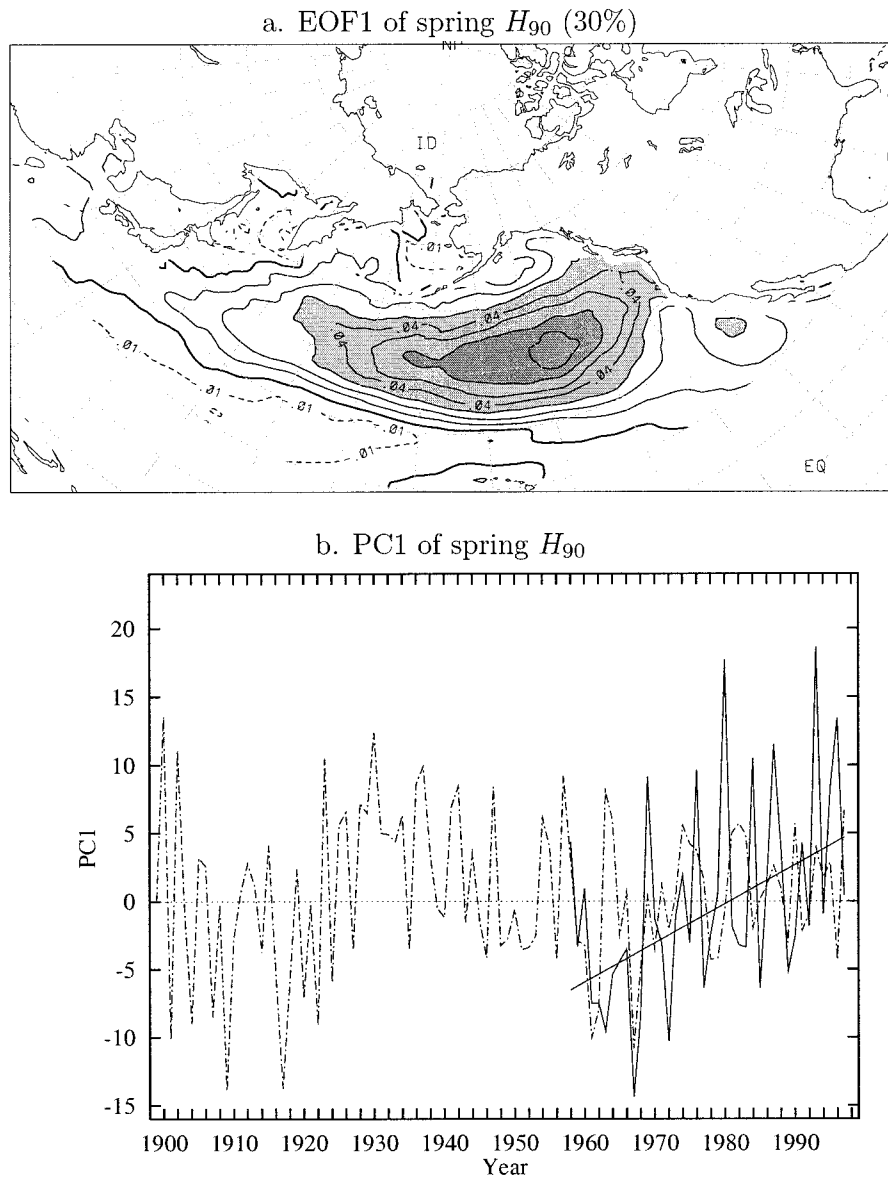


FIG. 9. The same as in Fig. 3 but for the EOF1 and PC1 of spring seasonal 90-percentiles of SWH (H_{90} , m) in the North Pacific.

in spring, resembles the trend pattern shown in Fig. 8b and the EOF1 shown in Fig. 9. This pair of predictor and predictand modes reveal that a deepened and eastward extended Aleutian low is associated with higher ocean wave heights (higher H_{90} values) in the central North Pacific. In the 1958–97 period, both the predictor and predictand time series possess a significant increasing trend. No significant trends are found in time series of other pairs of predictor and predictand modes.

For the spring H_{99} , similarly, the best predicted mode resembles the relevant trend pattern and EOF1. Higher H_{99} values in the central North Pacific are also found to be connected with a deepened and eastward extended Aleutian low; and vice versa. Both the predictor and

predictand time series have a significant increasing trend (figures look similar to those shown in Fig. 12 and hence are not shown here). The best predicted mode accounts for about 7% of the total H_{99} variance in spring.

As for the North Atlantic, the statistical reconstructions for the North Pacific also confirm the numerically hindcasted changes of oceanic wave extremes in the last four decades (cf. Figs. 9b and 11b). The reconstructed time series appear to possess notable variations on multidecadal timescales. However, significant changes are not identified from the 99-yr statistically reconstructed spring seasonal extremes (H_{90} and H_{99}) of SWH in the North Pacific.

In the winter season, the H_{99} and H_{90} appear to possess

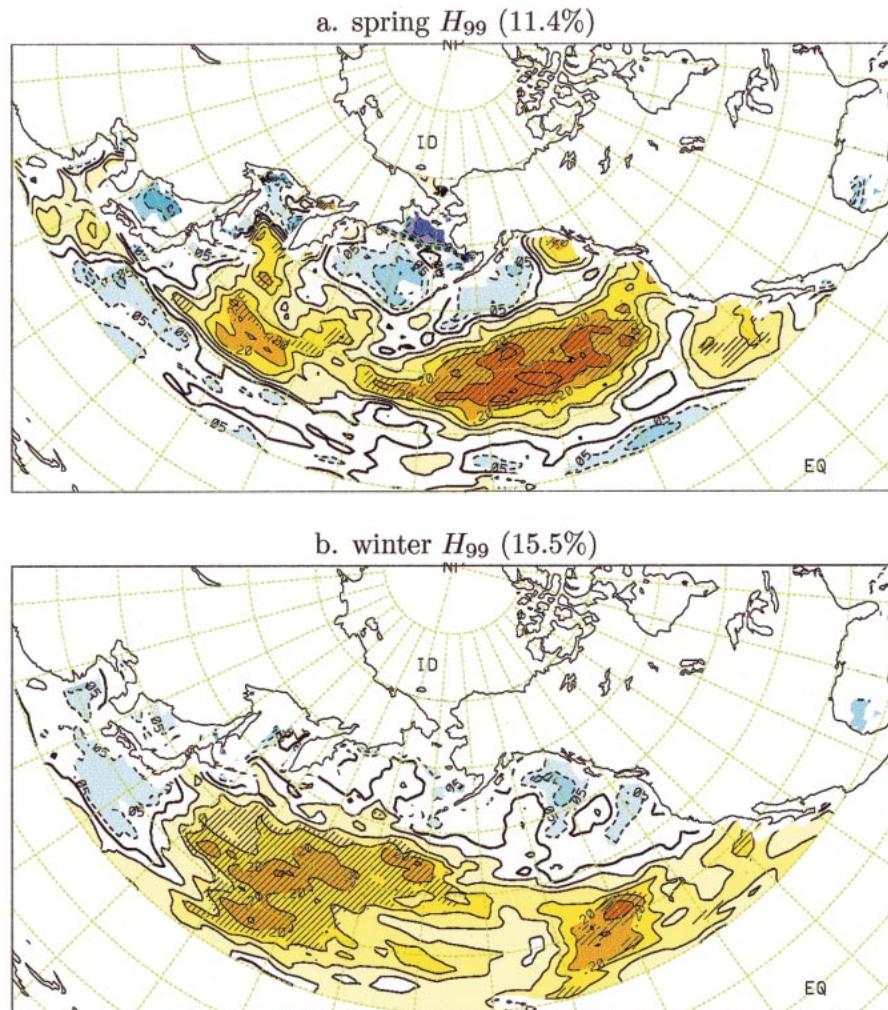


FIG. 10. The same as in Fig. 2 but for changes of the seasonal 99-percentiles of SWH (H_{99}) in the North Pacific in the spring and winter seasons, expressed as percentages of the relevant 40-yr mean H_{99} .

significant trends at least at the 90% confidence level. For example, as shown in Fig. 13, the EOF1 of the winter H_{99} resembles the trend pattern shown in Fig. 10b, and the associated PC1 possesses a significant increasing trend, representing significant increases in the central North Pacific. As shown in Fig. 14, the best predicted mode of the winter H_{99} also has a structure similar to the EOF1, accounting for about 19% of the total H_{99} variance in winter. This pair of predictor and predictand modes again reveals that significant increases of the winter H_{99} in the central North Pacific are associated with a deepened and eastward extended Aleutian low. In the last four decades, both the predictor and predictand time series possess a significant increasing trend. However, no significant trends are found in the 99-yr series of SLP or the reconstructed SWH extremes. Besides, both the predictor and predictand time series are significantly (at least at the 99% confidence level), negatively correlated with the seasonal Southern Os-

cillation index (i.e., the Tahiti-minus-Darwin normalized surface pressure index; Trenberth 1984). Consistent with this is the observation that the period of a deeper wintertime Aleutian low extends from 1977 to 1988, and during that period the tropical Pacific experienced above-normal SSTs (El Niño conditions) and a persistently negative Southern Oscillation index (Trenberth and Hurrell 1995; Nitta and Yamada 1989). Moreover, modeling studies (e.g., Blackmon et al. 1983; Alexander 1992) have confirmed the causal link between SSTs in the Tropics and the North Pacific circulation, with a deeper Aleutian low resulting from El Niño conditions.

As in the North Atlantic basin, trends in seasonal extremes of wind speed over the North Pacific are also similar to their SWH counterparts: Significant trends are identified for the winter and spring seasons, with the largest rate of increase (in percentage of the mean) being found in spring (cf. Fig. 15). These trend components are also found to be associated with the Aleutian low.

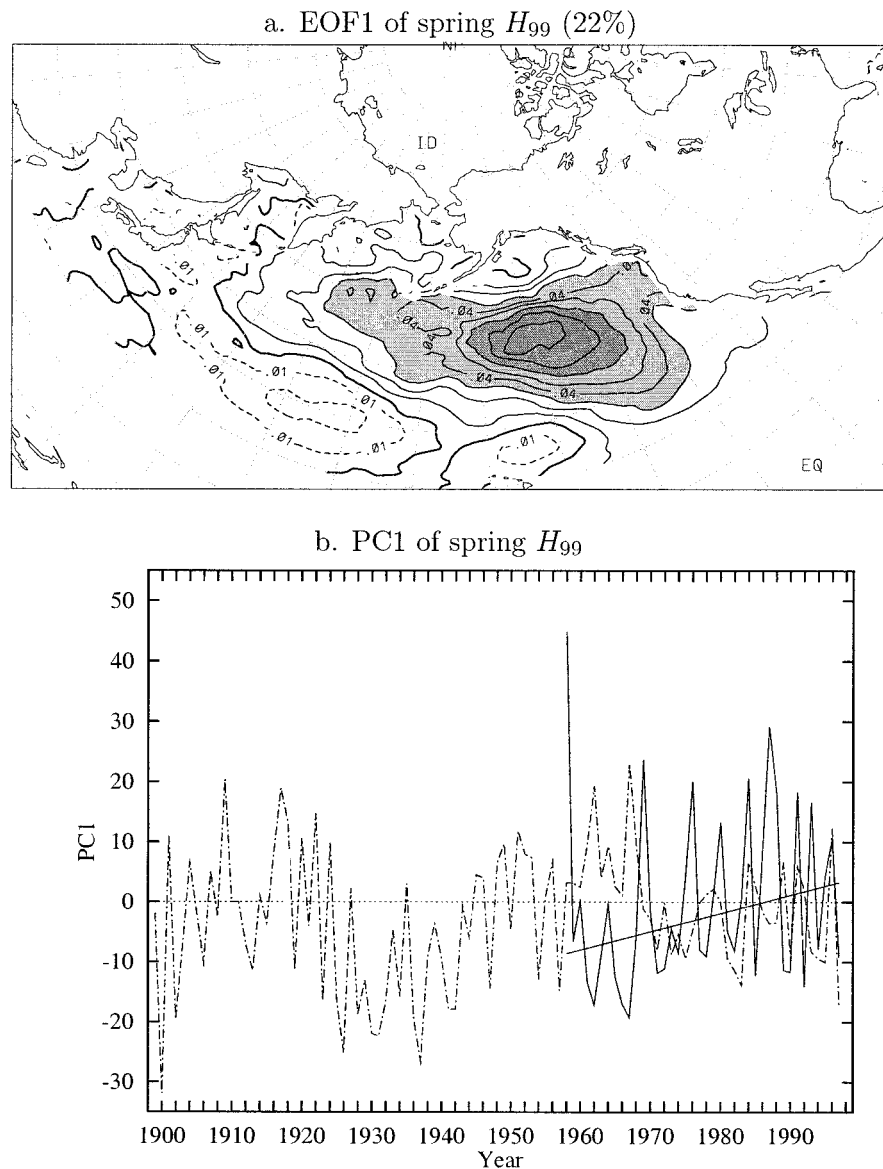


FIG. 11. The same as in Fig. 3 but for the EOF1 and PC1 of spring seasonal 99-percentiles of SWH (H_{99} , m) in the North Pacific.

In winter, however, the wind speed extremes appear to possess much less significant increases than the SWH counterparts, especially over the subtropical North Pacific (south of 30°N; cf. Fig. 15b and Fig. 8a).

5. Concluding remarks

Using the 40-yr (1958–97) numerical hindcast of significant wave height, we have identified significant linear trends in seasonal extremes (90- and 99-percentiles) of SWH for the North Atlantic and for the North Pacific. The relationships between the SWH extremes and the atmospheric circulation (SLP) patterns are also explored by performing Redundancy Analysis. Such relationships are then used to extend the 40-yr (1985–97) numerical

hindcast back to 1899, producing a 99-yr statistical hindcast of seasonal extremes of SWH. Thus, changes of SWH in the entire period of the last century are assessed. The significant trends in the SWH extremes are also linked to significant changes in the SLP fields. Since the SLP data are generally more homogeneous than the SWH data, the statistical hindcasts of SWH extremes provide a best guess of the temporal variations of SWH in the last century, and the SWH trends that are found to be associated with significant changes in the SLP fields can be considered to be more reliable.

In the North Atlantic, significant changes in seasonal extremes of SWH are found in the winter (JFM) season for the last four decades: significant increases in the northeast North Atlantic are matched by significant de-

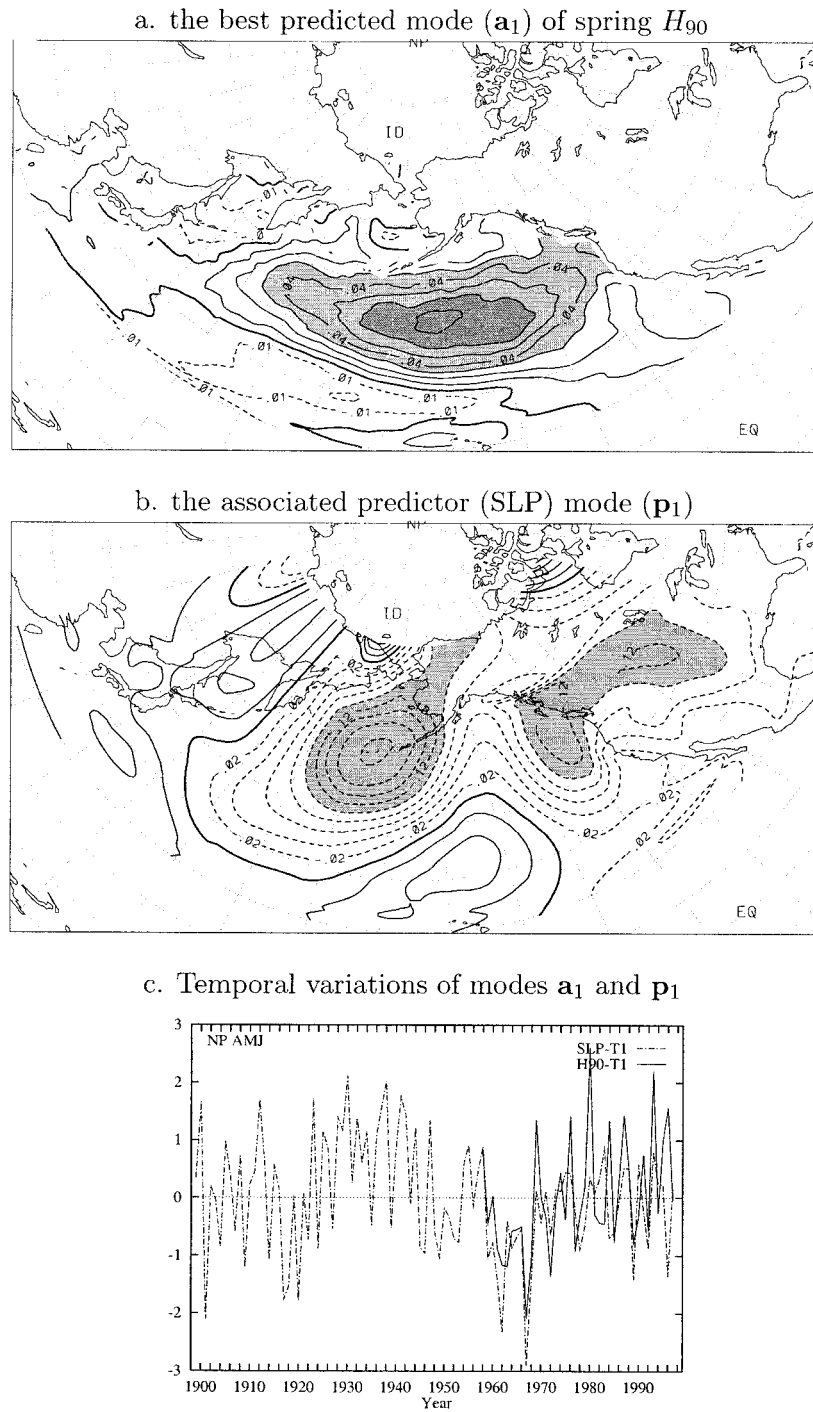


FIG. 12. The best predicted mode of spring seasonal 90-percentiles of SWH (H_{90}) in the North Pacific and the associated predictor (SLP) mode. In the 1958–97 period, both the predictor and the predictand time series (SLP-T1 and H90-T1; normalized) have a significant increasing trend.

creases in the subtropical North Atlantic. A similar trend pattern is also identified for the corresponding seasonal extremes of wind speed. Such trends are found to be closely connected with significant changes in the variability of the NAO. More specific, increases of the SWH

extremes in the northeast North Atlantic are found to be associated with an intensified Azores high and a deepened Icelandic low. This is consistent with the results of previous studies based on different datasets (Kushnir et al. 1997; The WASA group 1998).

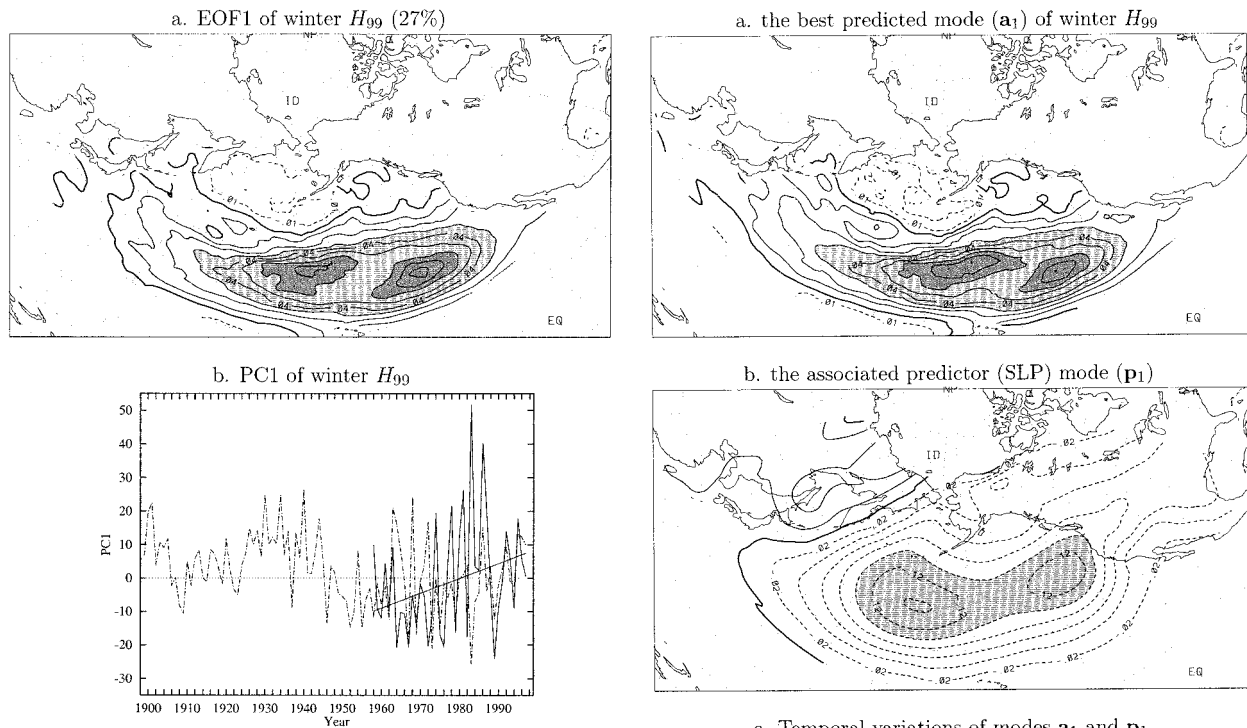


FIG. 13. The same as in Fig. 3 but for the EOF1 and PC1 of the winter seasonal 99-percentiles of SWH (H_{99} , m) in the North Pacific.

Extensive comparison of the results from this study with the previous three hindcasts described in section 1 is not possible because of the greatly differing length of record, time periods covered, areal domain, and statistics computed. Only Sterl et al. (1998) covered the North Pacific for instance, and only WASA covered a 40-yr period comparable to the present study. In addition, only WASA computed statistics for the 90- and 99-percentiles; the other two studies related to the mean SWH. Nevertheless some comparisons can be drawn. The present study shows similar patterns to Kushnir et al. (1997) in both the correlation pattern of SLP-SWH and in the rate of changes in the hindcast SWH. Comparisons with WASA can only be carried out in the northeast Atlantic, and the periods are slightly different, where the present hindcast extends a further three years, during a very active period. The trends in the 99-percentiles are up to about 3 cm yr^{-1} from WASA, and about 7 cm yr^{-1} in this study. Comparisons with Sterl et al. (1998) are more difficult because of both the very short length of their hindcast, and only having statistics on mean waves, for the winter season. Their North Atlantic patterns, however, are quite similar to ours.

The current study adds convincing support to the WASA group's conclusion that "the northeast North Atlantic has indeed roughened in recent decades, but the present intensity of the wave climate seems to be comparable with that at the beginning of this century." This study presents clearer pictures about changes in

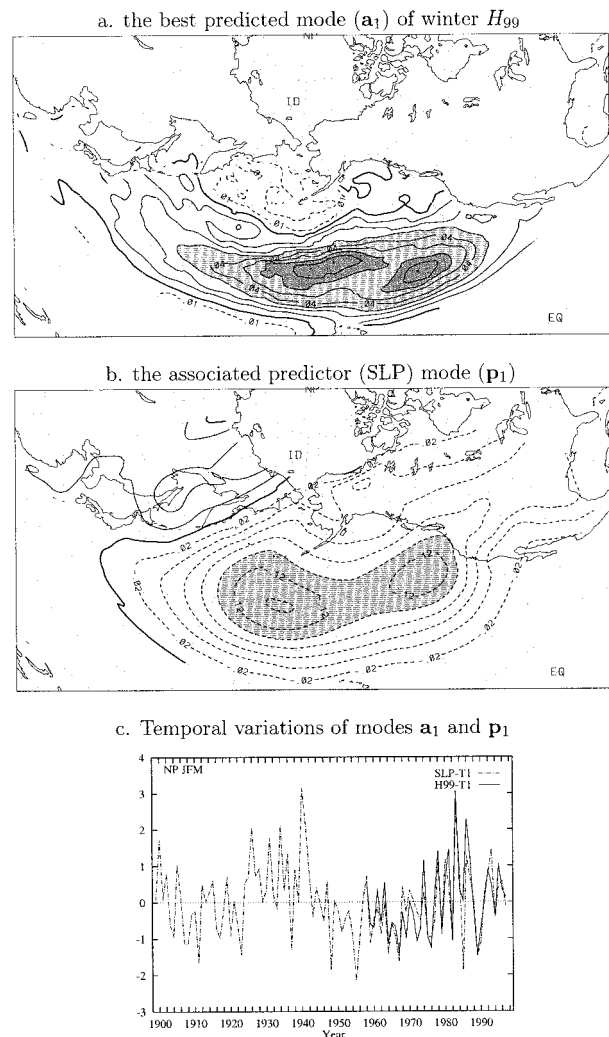


FIG. 14. The best predicted mode of winter seasonal 99-percentiles of SWH (H_{99}) in the North Pacific and the associated predictor (SLP) mode. In the 1958–97 period, both the predictor and the predictand time series (SLP-T1 and H_{99} -T1; normalized) have an increasing trend that is significant at least at the 90% confidence level.

extremes of SWH in the entire North Atlantic basin (north of 20°N) on a seasonal timescale, and about their connection to the changes in the NAO.

In the North Pacific, significant changes in seasonal extremes of SWH and wind speed are found in the spring (AMJ) season for the last four decades. In the winter (JFM) season, changes of SWH are also found to be significant at least at the 90% confidence level. The patterns found by Sterl et al. (1998) have some similarities to our results, especially the increases in the western Pacific, but their trend pattern is less pronounced and much noisier.

Trends of the SWH extremes in the North Pacific (NP) are related to changes of the Aleutian low: increases in the value of the SWH extremes in the central NP are found to be associated with a deeper and eastward extended Aleutian low.

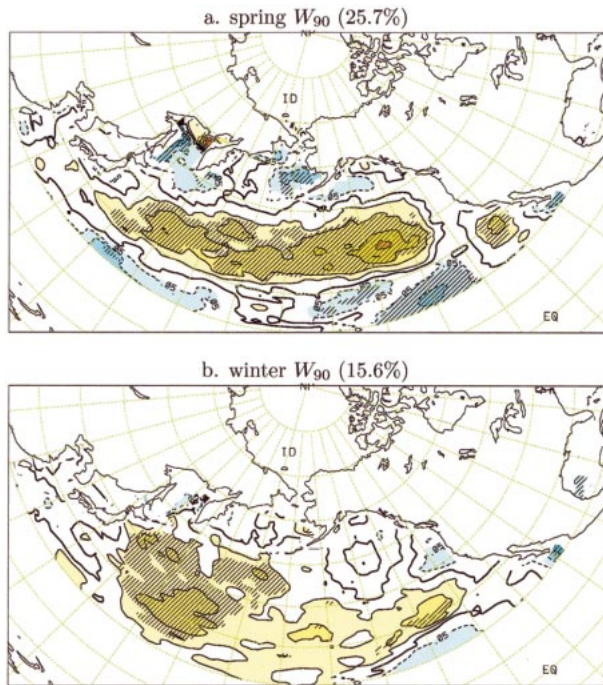


FIG. 15. The same as in Fig. 2 but for changes of the seasonal 90-percentiles of wind speed (W_{90}) in the North Pacific in the spring and winter seasons, expressed as percentages of the relevant 40-yr mean W_{90} .

For both the North Atlantic and the NP, no significant trends of the seasonal SWH extremes are found for the last century, though significant changes do exist in the last four decades. Nevertheless, long-term (multidecadal) fluctuations are quite noticeable, especially in the NP. The significant increases in the seasonal SWH extremes in the last few decades may well be due to the natural fluctuation. In addition, the connection between the SLP variations and the SWH extremes appears to be more apparent in the winter season than in other seasons.

Acknowledgments. The authors are grateful to Ain Naitsoo and Bjarne Hansen for preparing the wave data and to William D. Hogg for his thorough reading of the manuscript and helpful comments. Xuebin Zhang offered helpful suggestions and discussions during the course of this study, which are greatly appreciated. The editor Francis Zwiers and the two reviewers are also

TABLE 2. The rejection rates of the Mann–Kendall test on the seasonal 90- and 99-percentiles of SWH (H_{90} and H_{99}) in the North Atlantic and in the North Pacific. Here, trend could be field significant at the 5% level only if the rejection rate is greater than 12.5% (cf. section 3).

		Winter	Spring	Summer	Autumn
North Atlantic	H_{90}	15.5%	7.5%	10.3%	8.6%
	H_{99}	14.0%	5.1%	8.7%	9.5%
North Pacific	H_{90}	27.2%	24.4%	9.5%	7.7%
	H_{99}	15.5%	11.4%	4.2%	5.8%

acknowledged for their valuable comments and suggestions.

APPENDIX A

Techniques of Trend Analysis

The Mann–Kendall test (Mann 1945; Kendall 1955) is a nonparametric test for randomness against trend. According to Mann the null hypothesis of randomness H_0 states that the data (Y_1, Y_2, \dots, Y_n) are a sample of n independent and identically distributed random variables. The test statistic S is defined as

$$S = \sum_{k=1}^{n-1} \sum_{j=k+1}^n \text{sgn}(Y_j - Y_k), \tag{A1}$$

where

$$\text{sgn}(x) = \begin{cases} 1 & \text{if } x > 0, \\ 0 & \text{if } x = 0, \\ -1 & \text{if } x < 0. \end{cases} \tag{A2}$$

The distribution of S under H_0 is symmetrical and is normal in the limit as $n \rightarrow \infty$. Under H_0 , the mean of S is zero and, in case of no ties (e.g., no multiple values for the same sampling time), the variance of S is given by

$$V_S^2 = n(n-1)(2n+5)/18. \tag{A3}$$

A two-sided test for trend is then performed by comparing the following Z statistic:

$$Z = \begin{cases} (S-1)/V_S & \text{if } S > 0 \\ 0 & \text{if } S = 0 \\ (S+1)/V_S & \text{if } S < 0, \end{cases} \tag{A4}$$

with the critical value $Z_{\alpha/2}$ where $F_N(Z_{\alpha/2}) = \alpha/2$, F_N being the standard normal cumulative distribution function and α being the significance level for the test (Hirsch et al. 1982). The H_0 should be accepted if $|Z| \leq Z_{\alpha/2}$. A positive value of Z indicates an increasing trend, and a negative one a decreasing trend.

When trend exists, the time series can be described by linear regression $Y_t = a + bt + \varepsilon_t$, where ε_t denotes a white noise process, and a and b are regression parameters that are usually estimated using a least squares estimator. However, the least squares estimator of b is vulnerable to gross errors and the associated confidence interval is sensitive to nonnormality of the parent distribution (Sen 1968). In this study we use the estimator of b proposed by Sen (1968), which is based on Kendall’s rank correlation.

Without loss of generality we assume that $t_1 \leq t_2 \leq \dots \leq t_n$ are the sampling times which are not all equal. And let

$$N = \sum_{1 \leq i < j \leq n} \text{sgn}(t_j - t_i), \tag{A5}$$

where $\text{sgn}(x)$ is as defined in (A2). Then, among all

values of $(t_j - t_i)$, $1 \leq i \leq j \leq n$, only N values are nonzero. We now consider the set \mathcal{R} of N distinct pairs (i, j) for which $t_j > t_i$, and define

$$X_{ij} = (Y_j - Y_i)/(t_j - t_i), \quad (i, j) \in \mathcal{R} \quad (\text{A6})$$

We then arrange the N values in (A6) in ascending order of magnitude and denote the k th smallest value by X_k ($k = 1, 2, \dots, N$). Thus, the estimator of b based on Kendall's rank correlation is given by

$$\hat{b} = \begin{cases} X_{(N-1)/2+1} & \text{if } N \text{ is odd,} \\ (X_{N/2} + X_{N/2+1})/2 & \text{if } N \text{ is even.} \end{cases} \quad (\text{A7})$$

Let $N^* = Z_{\alpha/2} V_S$, and $M_1 = (N - N^*)/2$ and $M_2 = (N + N^*)/2$. Then (X_{M_1}, X_{M_2+1}) gives the $(1 - \alpha)$ confidence interval of estimator \hat{b} .

Another problem arises here. The result of the Mann-Kendall test depends strongly on the autocorrelation. If there is a positive autocorrelation in the time series, the test rejects the null hypothesis H_0 more often than specified by the significance level (von Storch and Navarra 1995). In other words, the test would increase the apparent level of significance of trend in a time series. To eliminate this effect of autocorrelation, we first calculated the partial correlations (for lag = 1, 2, ..., 10) of the time series in question (say, Y_t). As a result, we found that, for the time series under investigation in this study, few partial correlations at lag > 1 are significant at the (approximately) 5% level. Thus, we then "prewhiten" the time series in question and estimate its trend component by fitting the following model

$$Y_t = a + bt + X_t, \quad (\text{A8})$$

where a and b are the intercept and slope (trend) parameters of Y_t , and X_t is a red noise process of lag-1 autocorrelation c :

$$X_t = cX_{t-1} + \varepsilon_t. \quad (\text{A9})$$

With this model, it is easily shown that

$$Y_t - cY_{t-1} = [(1 - c)a + cb] + [(1 - c)b]t + \varepsilon_t. \quad (\text{A10})$$

A prewhitened time series that possesses the same trend as does the original time series Y_t can be obtained as

$$W_t = (Y_t - cY_{t-1})/(1 - c) = a' + bt + \varepsilon_t, \quad (\text{A11})$$

where $a' = a + cb/(1 - c)$, and $\varepsilon_t = \varepsilon_t/(1 - c)$ is a white noise process. This prewhitened time series W_t is considerably less plagued by serial correlation.

Since trend and autocorrelation often concur in a time series, we estimate the autocorrelation c and regression coefficient b by adopting an "iteration" scheme as follows:

- 1) We compute the lag-1 autocorrelation \hat{c}_0 of the time series Y_t as a first estimate of c . If $\hat{c} < 0.05$, the effect of serial correlation is negligible (cf. von Storch and Navarra 1995), we can simply use the above described estimator to estimate regression pa-

rameter b from the original time series Y_t and no iteration is necessary. Otherwise, we perform the above described trend analysis on the prewhitened time series $W_t = (Y_t - \hat{c}_0 Y_{t-1})/(1 - \hat{c}_0)$, obtaining a first estimate of b , say \hat{b}_0 .

- 2) We remove the estimated trend component from the original data series and reestimate c . In other words, our new estimate \hat{c}_1 is the lag-1 autocorrelation of time series $(Y_t - \hat{b}_0 t)$. If $\hat{c}_1 < 0.05$, we take $\hat{c} = \hat{c}_0$ and $\hat{b} = \hat{b}_0$ as the final estimates of c and b and stop the iteration. Otherwise, we perform the trend analysis on the prewhitened times series $W_t = (Y_t - \hat{c}_1 Y_{t-1})/(1 - \hat{c}_1)$, obtaining a new estimate of b , say \hat{b}_1 .
- 3) If $|\hat{c}_1 - \hat{c}_0|$ and $|\hat{b}_1 - \hat{b}_0|$ are smaller than a specified tiny number (e.g., 0.0001), we stop the iteration and take \hat{c}_1 and \hat{b}_1 as the final estimates of c and b , respectively (i.e., $\hat{c} = \hat{c}_1$ and $\hat{b} = \hat{b}_1$). Otherwise, we set $\hat{c}_0 = \hat{c}_1$ and $\hat{b}_0 = \hat{b}_1$, and repeat 2 and 3. Once we have obtained appropriate estimates \hat{c} and \hat{b} , we use the least squares estimator to estimate the parameter a from the prewhitened times series $W_t = (Y_t - \hat{c} Y_{t-1})/(1 - \hat{c})$. The Mann-Kendall test on this prewhitened time series concludes the trend analysis.

APPENDIX B

Redundancy Analysis

Like Canonical Correlation Analysis (CCA), RA (von Storch and Zwiers 1999; Tyler 1982) is a technique that is used to associate patterns of variation in a predictor field with patterns of the predictand field through a regression model. It differs from CCA because it seeks to find pairs of predictor and predictand patterns that maximize the associated predictand variance, rather than the correlation only.

Since a detailed description of RA can be found in Wang and Zwiers (2001), von Storch and Zwiers (1999), and Tyler (1982), only a briefly description of this technique is provided here.

Let \mathbf{X} and \mathbf{Y} be a pair of random vectors with dimensions M_X and M_Y , respectively. Further, let \mathbf{C}_{XX} and \mathbf{C}_{YY} be the covariance matrices of \mathbf{X} and \mathbf{Y} respectively, and let \mathbf{C}_{XY} and \mathbf{C}_{YX} be their cross-covariance matrices. The regression of \mathbf{Y} on \mathbf{X} is given by

$$\hat{\mathbf{Y}} = \mu_Y + \mathbf{C}_{YX} \mathbf{C}_{XX}^{-1} (\mathbf{X} - \mu_X) \quad (\text{B1})$$

where $\hat{\mathbf{Y}}$ is the linear prediction of \mathbf{Y} by \mathbf{X} , and μ_X and μ_Y are the expected values of \mathbf{X} and \mathbf{Y} , respectively. It is easily shown that the covariance matrix of $\hat{\mathbf{Y}}$ is $\mathbf{C}_{\hat{Y}\hat{Y}} = \mathbf{C}_{YX} \mathbf{C}_{XX}^{-1} \mathbf{C}_{XY}$.

Using training datasets of \mathbf{X} and \mathbf{Y} , we can easily obtain estimates of the parameters in (B1) and hence the linear predictions $\hat{\mathbf{Y}}$. The EOFs of $\hat{\mathbf{Y}}$ are then estimated by solving the eigen-equation

$$\mathbf{C}_{\hat{Y}\hat{Y}} \mathbf{a}_j = \lambda_j \mathbf{a}_j, \quad (\text{B2})$$

where the nonzero eigenvalues λ_j s and associated EOFs

\mathbf{a}_j s are ordered so that $\lambda_1 \geq \lambda_2 \geq \dots \geq \lambda_K > 0$. Then, mode \mathbf{a}_j is the j th best predicted mode of the predictand, also referred to as the j th RA mode ($j = 1, 2, \dots, K$). Here $\mathbf{A} = [\mathbf{a}_1, \mathbf{a}_2, \dots, \mathbf{a}_K]$ is an orthonormal transformation. The j th best predicted component is given as $\mathbf{a}_j^T \hat{\mathbf{Y}}$, which describes the temporal variation of mode \mathbf{a}_j .

The so-called redundancy index is defined as

$$\begin{aligned} R^2(\mathbf{Y} : \mathbf{X}) &= R^2(\mathbf{Y} : \hat{\mathbf{Y}}) = \frac{\text{trace}(\mathbf{C}_{\hat{\mathbf{Y}}\hat{\mathbf{Y}}})}{\text{trace}(\mathbf{C}_{\mathbf{Y}\mathbf{Y}})} \\ &= \sum_{j=1}^K R^2(\mathbf{Y} : \mathbf{a}_j^T \hat{\mathbf{Y}}). \end{aligned} \quad (\text{B3})$$

Apparently, this index represents the proportion of the total variance in \mathbf{Y} , which can be accounted for by the linear prediction $\hat{\mathbf{Y}}$.

Further, let $\mathbf{B} = [\mathbf{b}_1, \mathbf{b}_2, \dots, \mathbf{b}_K]$ where

$$\mathbf{b}_j = \lambda_j^{-1/2} \mathbf{C}_{\mathbf{X}\mathbf{X}}^{-1} \mathbf{C}_{\mathbf{X}\mathbf{Y}} \mathbf{a}_j. \quad (\text{B4})$$

Then, \mathbf{B} is a nonsingular matrix; and we have the following expansions: $\hat{\mathbf{Y}} = \mathbf{A}(\mathbf{A}^T \hat{\mathbf{Y}})$ and $\mathbf{X} = \mathbf{P}(\mathbf{B}^T \mathbf{X})$ where $\mathbf{P}^T = [\mathbf{p}_1, \mathbf{p}_2, \dots, \mathbf{p}_K]^T = \mathbf{B}^{-1}$, \mathbf{p}_j being the j th predictor pattern that forecasts mode \mathbf{a}_j ($j = 1, 2, \dots, K$). The temporal variation of mode \mathbf{p}_j is described by time series $\mathbf{b}_j^T \mathbf{X}$. Thus, RA allows us to associate a hierarchy of best predicted orthogonal modes \mathbf{a}_j with the relevant predictor patterns \mathbf{p}_j ($j = 1, 2, \dots, K$).

REFERENCES

- Alexander, M., 1992: Midlatitude atmosphere–ocean interaction during El Niño. Part II. The Northern Hemisphere atmosphere. *J. Climate*, **5**, 959–972.
- Blackmon, M. L., J. E. Geisler, and E. J. Pitcher, 1983: A general circulation model study of January climate anomaly patterns associated with interannual variation of equatorial Pacific sea surface temperatures. *J. Atmos. Sci.*, **40**, 1410–1425.
- Cardone, V. J., and D. T. Resio, 1998: An assessment of wave modeling technology. *Proc. Fifth Int. Workshop on Wave Hindcasting and Forecasting*, Melbourne, FL, Environment Canada, 468–492.
- , W. J. Pierson, and E. G. Ward, 1976: Hindcasting the directional spectrum of hurricane-generated waves. *J. Petrol. Technol.*, **28**, 385–394.
- , R. E. Jensen, D. T. Resio, V. R. Swail, and A. T. Cox, 1996: Evaluation of contemporary ocean wave models in rare extreme events: The “Halloween Storm” of October 1991 and the “Storm of the Century” of March, 1993. *J. Atmos. Oceanic Technol.*, **13**, 198–230.
- Cox, A. T., and V. R. Swail, 2001: A global wave hindcast in the period 1958–1997: Validation and climate assessment. *J. Geophys. Res.*, in press.
- Gibson, R., P. Kallberg, and S. Uppala, 1996: The ECMWF Reanalysis (ERA) Project. *ECMWF Newsl.*, **73**, 7–17.
- Greenwood, J. A., V. J. Cardone, and L. M. Lawson, 1985: Intercomparison test version of the SAIL wave model. *Ocean Wave Modelling*, the SWAMP group. Plenum Press, 221–233.
- Gunther, H., W. Rosenthal, M. Stawarz, J. C. Carretero, M. Gomez, I. Lozano, O. Serano, and M. Reistad, 1998: The wave climate of the Northeast Atlantic over the period 1955–1994: The WASA wave hindcast. *Global Atmos. Oceanic System*, **6**, 121–163.
- Hirsch, R. M., J. R. Slack, and R. A. Smith, 1982: Techniques of trend analysis for monthly water quality data. *Water Resour. Res.*, **18**, 107–121.
- Hurrell, J. W., 1995: Decadal trends in the North Atlantic Oscillation: Regional temperatures and precipitation. *Science*, **269**, 676–679.
- Kalnay, E., and Coauthors, 1996: The NCEP/NCAR 40-year reanalysis project. *Bull. Amer. Meteor. Soc.*, **77**, 437–471.
- Kendall, M. G., 1955: *Rank Correlation Methods*. Charles Griffin, 196 pp.
- Khandekar, M. L., R. Lalbeharry, and V. J. Cardone, 1994: The performance of the Canadian Spectral Ocean Wave Model (CSOWM) during the Grand Banks ERS-1 SAR Wave Spectra Validation Experiment. *Atmos.–Ocean*, **31**, 31–60.
- Kushnir, Y., V. J. Cardone, J. G. Greenwood, and M. A. Cane, 1997: The recent increase in North Atlantic wave heights. *J. Climate*, **10**, 2107–2113.
- Lambert, S. J., 1996: Intense extratropical northern hemisphere winter cyclone events: 1899–1991. *J. Geophys. Res.*, **101**, 21 319–21 325.
- Livezey, R. E., and W. Y. Chen, 1983: Statistical field significance and its determination by Monte Carlo techniques. *Mon. Wea. Rev.*, **111**, 46–59.
- Mann, H. B., 1945: Non-parametric tests against trend. *Econometrica*, **13**, 245–259.
- Nitta, T., and S. Yamada, 1989: Recent warming of tropical sea surface temperature and its relationship to the Northern Hemisphere Circulation. *J. Meteor. Soc. Japan*, **67**, 375–383.
- Schinke, H., 1993: On the occurrence of deep cyclones over Europe and the North Atlantic in the period 1930–1991. *Beitr. Phys. Atmosph.*, **66**, 223–237.
- Schmith, T., E. Kaas, and T.-S. Li, 1998: Northeast Atlantic winter storminess 1875–1995 re-analysed. *Climate Dyn.*, **14**, 529–536.
- Sen, P. K., 1968: Estimates of the regression coefficient based on Kendall’s tau. *J. Amer. Statist. Assoc.*, **63**, 1379–1389.
- Sterl, A., G. J. Komen, and P. D. Cotton, 1998: Fifteen years of global wave hindcasts using winds from the European Centre for Medium-Range Weather Forecasts reanalysis: Validating the reanalyzed winds and assessing the wave climate. *J. Geophys. Res.*, **103**, 5477–5492.
- Swail, V. R., and A. T. Cox, 2000: On the use of NCEP–NCAR reanalysis surface marine wind fields for a long-term North Atlantic wave hindcast. *J. Atmos. Oceanic Technol.*, **17**, 532–545.
- Trenberth, K. E., 1984: Signal versus noise in the Southern Oscillation. *Mon. Wea. Rev.*, **112**, 326–332.
- , and D. A. Paolino Jr., 1980: The Northern Hemisphere sea-level pressure dataset: Trends, errors, and discontinuities. *Mon. Wea. Rev.*, **108**, 855–872.
- , and J. W. Hurrell, 1995: Decadal climate variations in the Pacific. *Natural Climate Variability on Decade-to-Century Time Scales*, D. G. Martinson, et al., Eds. National Academy Press, 472–482.
- Tyler, D. E., 1982: On the optimality of the simultaneous redundancy transformations. *Psychometrika*, **47**, 77–86.
- von Storch, H., and A. Navarra, 1995: *Analysis of Climate Variability—Applications of Statistical Techniques*. Springer-Verlag, 334 pp.
- , and F. W. Zwiers, 1999: *Statistical Analysis in Climate Research*. Cambridge University Press, 484 pp.
- Wang, X. L., and F. W. Zwiers, 2001: Using redundancy analysis to improve dynamical seasonal mean 500-hPa geopotential forecasts. *Int. J. Climatol.*, in press.
- WASA, 1998: Changing waves and storms in the northeast Atlantic? *Bull. Amer. Meteor. Soc.*, **79**, 741–760.